



Article

# Fast and Facile Synthesis of Pt Nanoparticles Supported on Ketjen Black by Solution Plasma Sputtering as Bifunctional HER/ORR Catalysts

Chitlada Mani-Lata <sup>†</sup>, Chadapat Hussakan <sup>†</sup> and Gasidit Panomsuwan <sup>\*†</sup>

Department of Materials Engineering, Faculty of Engineering, Kasetsart University, Bangkok 10900, Thailand; chitlada.ma@ku.th (C.M.-L.); chadapat.h@ku.th (C.H.)

\* Correspondence: gasidit.p@ku.ac.th; Tel.: +66-2797-0999

<sup>†</sup> These authors contributed equally to this work.

Received: 29 June 2020; Accepted: 18 August 2020; Published: 19 August 2020



**Abstract:** Hydrogen evolution reaction (HER) and oxygen reduction reaction (ORR) are two core electrochemical processes involved in hydrogen fuel cell (HFC) technology. ORR is a cathodic reaction occurring in HFC, whereas HER can convert the H<sub>2</sub>O byproduct from HFCs into H<sub>2</sub> gas via water splitting. Platinum (Pt)-based catalysts are the most effective catalysts for both reactions. In this work, we used a fast, facile, and chemical-free method, called solution plasma sputtering (SPS), to synthesize Pt nanoparticles supported on Ketjen Black (KB). The discharge time was varied (5, 10, and 20 min) to alter the Pt loading. Characterization results revealed that the plasma did not affect the morphology of KB, and the Pt loading on KB increased with increasing discharge time (5.5–17.9 wt%). Well-crystallized Pt nanoparticles, ~2–5 nm in diameter, were obtained. Electrochemical measurements revealed that Pt/KB exhibited bifunctional catalytic activity toward HER and ORR in 0.5 M H<sub>2</sub>SO<sub>4</sub> solution. Both HER and ORR activities enhanced as the loading of Pt nanoparticles increased with a longer discharge time. Moreover, Pt/KB exhibited better HER and ORR stability than a commercial Pt-based catalyst, which was attributed to the stronger adhesion between Pt nanoparticles and KB support. Thus, SPS can be applied as an alternative synthesis method for preparing Pt/KB catalysts for HER and ORR.

**Keywords:** hydrogen fuel cells; electrocatalysts; Pt nanoparticles; solution plasma sputtering; oxygen reduction reaction; hydrogen evolution reaction

## 1. Introduction

Fossil fuels are exhaustible natural resources and induce climate change by generating carbon monoxide (CO), carbon dioxide (CO<sub>2</sub>), and other greenhouse gases when burned. Recently, numerous studies have devoted particular attention to renewable and sustainable energy sources, including solar [1], wind [2], biogas [3], and hydrogen [4], as replacements for fossil fuels. Hydrogen fuel cell (HFC) is recognized as an efficient alternative energy source to rival fossil fuels in the near future because it can be practically used in portable devices, vehicles, and stationary power systems [5–9].

In the operation of a HFC, H<sub>2</sub> gas is fed to the anode to promote hydrogen oxidation reaction (HOR), where H<sub>2</sub> molecules are separated into protons and electrons on catalysts ( $\text{H}_2 \rightarrow 2\text{H}^+ + 2\text{e}^-$ ). The electrons produced from the anode flow to an external circuit, thus creating electricity, while protons migrate through the membrane to the cathode. Conversely, the cathode is supplied with O<sub>2</sub> gas. The oxygen reduction reaction (ORR) occurs through proton reaction with O<sub>2</sub> and electrons ( $4\text{H}^+ + \text{O}_2 + 4\text{e}^- \rightarrow 2\text{H}_2\text{O}$ ), producing H<sub>2</sub>O as a byproduct. Therefore, the HFC is a clean energy source with zero emissions of toxic gases. Compared with HOR, the ORR plays a more significant role in determining the performance and durability of HFCs [10–12].

Currently, H<sub>2</sub> gas production can be categorized into four technologies: (i) thermochemical, (ii) electrochemical, (iii) photobiological, and (iv) photoelectrochemical [13]. Using the steam reforming process, thermochemical technology is the most widely used method for producing H<sub>2</sub> from natural gas, coal, methanol, and gasoline. However, CO production requires one or more subsequent steps to convert CO into CO<sub>2</sub> [14]. Electrochemical water splitting is a well-known clean and sustainable technology producing H<sub>2</sub> gas via the hydrogen evolution reaction (HER,  $2\text{H}^+ + 2\text{e}^- \rightarrow \text{H}_2$ ) at the cathode [15,16]. Therefore, the H<sub>2</sub>O byproduct from HFC operation can be converted back to H<sub>2</sub> gas to self-supply the anode. Moreover, the use of H<sub>2</sub>O as a source for H<sub>2</sub> production can solve the problem of the H<sub>2</sub> storage system, which requires high costs and safety levels for transportation [17,18].

In this context, HER and ORR are two core electrochemical processes in achieving full implementation of HFC technology. Among active catalyst materials, platinum (Pt) is the most efficient catalyst for both HER and ORR [19–22]. In practical use, Pt nanoparticles (2–5 nm) are loaded onto various kinds of material supports (e.g., carbon black [23], carbon nanotubes [24], graphene [25], or metal oxide [26]) for use as HER/ORR catalysts. The most common method for synthesizing Pt nanoparticles relies on the bottom-up chemical reduction in water-soluble Pt<sup>2+</sup> or Pt<sup>4+</sup> ions as precursors (e.g., H<sub>2</sub>PtCl<sub>6</sub>, K<sub>2</sub>PtCl<sub>4</sub>, PtCl<sub>4</sub>, and Pt(AcAc)<sub>2</sub>). The Pt<sup>2+/4+</sup> ions are reduced to Pt<sup>0</sup> using a reducing agent (e.g., NaBH<sub>4</sub> or KC<sub>4</sub>H<sub>5</sub>O<sub>6</sub>) and subsequently grow into particles. The size and shape of the synthesized Pt nanoparticles can be controlled by adjusting the reaction temperature, reducing agent, and Pt precursor concentration [27,28]. However, this method has some drawbacks: it is a multistep process, involves long processing times, requires reducing/capping agents, and usually requires subsequent purification of the product. Moreover, the residual organic capping layer on the surface of Pt nanoparticles can inhibit and reduce their catalytic activity [29–31]. Thus, chemical bonding between organic capping layers and nanoparticle surfaces plays a substantial role in determining the catalytic activity of Pt nanoparticles. Therefore, a method for the simple, fast, and chemical-free synthesis of Pt nanoparticles is urgently needed in the catalysis field.

Recently, solution plasma sputtering (SPS) has emerged as a powerful approach to synthesize various noble metal nanoparticles through a direct sputtering from a highly pure metallic electrode (e.g., Au [32], Pt [33], Ag [34], Pd [35], or AuPt [36]) without using a chemical reducing agent. Solution plasma is defined as a nonequilibrium plasma or cold plasma generated in a liquid solution at room temperature and atmospheric pressure. A high voltage with short-pulsed duration and high frequency is typically used to generate plasma [37]. The size of the obtained metal nanoparticles ranges from 2 to 10 nm, depending on the plasma conditions and liquid medium. The synthesis time is typically 5–30 min, which is faster than the conventional chemical reduction process. Importantly, the surface of the Pt nanoparticles is clean, without an organic layer, because of the chemical-free synthesis. Therefore, the Pt nanoparticles synthesized using SPS should have strong potential for catalyzing HER and ORR.

Herein, Pt nanoparticles were synthesized using SPS through sputtering of Pt electrodes submerged in a solution with dispersed carbon black (Ketjen black (KB), EC600JD). The Pt nanoparticles sputtering from the electrodes migrate and deposit onto the KB surface, resulting in a Pt/KB composite system. The loading of Pt nanoparticles on KB was varied by adjusting the discharge time (5–20 min). The morphology, crystal structure, and surface area of Pt/KB were evaluated using several characterization techniques, such as field-emission scanning electron microscopy (FE-SEM), transmission electron microscopy (TEM), X-ray diffraction (XRD), and surface-area analysis. The quantity and dispersion of Pt nanoparticles on KB were characterized using energy-dispersive X-ray spectroscopy (EDX) analysis. To evaluate HER and ORR, cyclic voltammetry (CV) and linear sweep voltammetry (LSV) measurements were performed using a three-electrode system in both N<sub>2</sub>- and O<sub>2</sub>-saturated 0.5 M sulfuric acid (H<sub>2</sub>SO<sub>4</sub>) solutions.

## 2. Materials and Methods

### 2.1. Materials

Pt wire (diameter 0.8 mm, purity 99.99%) was purchased from Nilaco Corp. (Tokyo, Japan). Ethanol ( $C_2H_5OH$ , purity 99.9%), isopropanol ( $C_3H_8O$ , purity 99.8%), and 0.5 M  $H_2SO_4$  were obtained from RCI Labscan Ltd. (Bangkok, Thailand). Then, 20-wt% Pt on Vulcan XC-72 (20% Pt/VC) and Nafion<sup>®</sup> DE 521 solution (5 wt% in a mixture of lower aliphatic alcohols and water) were obtained from Sigma-Aldrich. Ultrapure water (18.2 M $\Omega$  cm at 25 °C) was obtained from a Direct-Q<sup>™</sup> 5 UV Millipore water purification system. All the chemicals were of analytical grade and were used without further purification.

### 2.2. Preparation of Pt/KB Catalysts by SPS

Fifty milligrams of KB was placed in a mixture of ethanol (40 mL) and ultrapure water (40 mL). The mixture was stirred at 500 rpm for 30 min, followed by sonication in an ultrasonic bath for 30 min to obtain a homogeneous dispersion. The experimental setup is illustrated in Figure 1a. A pair of Pt wires covered with an insulating ceramic tube was set with a gap distance of 0.5 mm at the center of a glass beaker. The as-prepared mixture was poured into the beaker and constantly stirred at 500 rpm. A bipolar-pulse voltage was supplied to the Pt electrodes using an MPP-HV04 Pekuris bipolar pulse generator (Kurita Seisakusho Co., Ltd., Kyoto, Japan). The frequency and pulse duration were fixed at 20 kHz and 0.8  $\mu$ s, respectively. The discharge time was varied at 5, 10, and 20 min. Once the plasma was generated, the Pt nanoparticles were produced by sputtering from the Pt electrode surface. The Pt nanoparticles diffused from the plasma zone to the liquid phase and then deposited onto the KB support, resulting in *t*-Pt/KB composites, where *t* represents the discharge time (Figure 1b). The Pt/KB samples were collected by vacuum filtration using Whatman No. 1 filter paper and then dried in a hot-air oven (Memmert UN-55) at 100 °C for 12 h. After drying, the Pt/KB samples were ready for further characterization and electrochemical measurements.

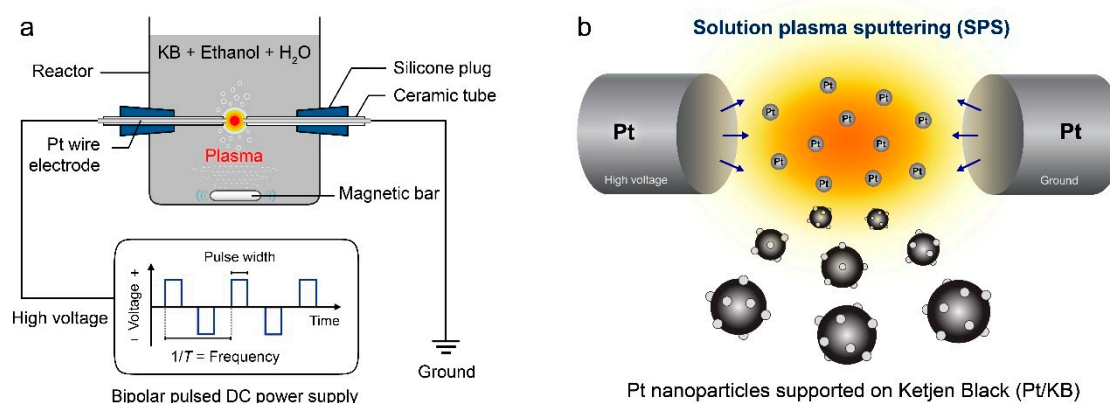


**Figure 1.** (a) Schematic of the experimental setup of the solution plasma sputtering (SPS) for the preparation of Pt/KB catalysts; (b) enlarged view at the electrode gap, showing the production of Pt nanoparticles from electrodes and deposition on the KB supports.

### 2.3. Characterization

The morphology of catalysts was examined using a JEOL JSM-7600F field-emission scanning electron microscope operating at an acceleration voltage of 1 kV. The quantity and dispersion of Pt nanoparticles on KB were evaluated on an Oxford Instruments AZtecOne spectrometer. The size of the Pt nanoparticles on the KB was investigated using a JEOL JEM-3100F transmission electron microscope operated at an acceleration voltage of 300 kV. Thermogravimetric analysis (TGA) was performed on a Mettler Toledo TGA2 thermogravimetric analyzer to evaluate the Pt loading. The samples were heated

from 50 °C to 900 °C with a heating rate of 10 °C min<sup>-1</sup> under air flow. Fourier transform infrared spectroscopy (FTIR) spectra were collected using a Bruker Alpha-E spectrometer in the range of 500–4000 cm<sup>-1</sup>. XRD patterns of catalysts were recorded on a Bruker D8 Advance X-ray diffractometer using a Cu K $\alpha$  radiation source ( $\lambda = 1.54 \text{ \AA}$ ) in the 2 $\theta$  range of 10°–80° at a scan rate of 3° min<sup>-1</sup>. The specific surface area of all catalysts was determined from N<sub>2</sub> adsorption–desorption isotherms recorded at liquid-N<sub>2</sub> temperature (77 K) using a Micromeritics 3Flex surface characterization analyzer. Before measurements, the catalysts were degassed at 150 °C for 6 h under vacuum.

#### 2.4. Electrode Preparation

The catalyst suspension was prepared by dispersing 5-mg catalyst in a mixture of ultrapure water (475  $\mu\text{L}$ ), isopropanol (475  $\mu\text{L}$ ), and Nafion (50  $\mu\text{L}$ ). The resulting suspension (5 mg mL<sup>-1</sup>) was sonicated in an ultrasonic bath until a well-dispersed ink was obtained. A glassy carbon electrode (3-mm diameter, 0.071-cm<sup>2</sup> area) was successively polished on a polishing pad with diamond (1  $\mu\text{m}$ ) and alumina slurries (0.05  $\mu\text{m}$ ), followed by cleaning with water in an ultrasonic bath for 5 min. Three microliters of catalyst ink of each sample was then carefully dropped onto the cleaned glassy carbon electrodes and left in ambient air condition until completely dry. The catalyst loading was 0.212 mg cm<sup>-2</sup>. A commercial 20% Pt/VC was also used as a benchmark catalyst for comparison.

#### 2.5. HER and ORR Activity Measurements

The HER and ORR activities of all catalysts were evaluated in a 0.5 M H<sub>2</sub>SO<sub>4</sub> solution using a three-electrode system. A catalysts-modified glassy carbon electrode was used as the working electrode. A Pt wire and Ag/AgCl (saturated KCl) electrode were used as the counter and reference electrodes, respectively. The measured electrode potentials vs. Ag/AgCl were converted into the reversible hydrogen electrode (RHE) scale using  $E_{\text{RHE}} = E_{\text{Ag/AgCl}} + 0.197 \text{ V} + 0.059(\text{pH})$ . Three electrodes were connected to a Biologic VSP potentiostat controlled by the EC-Lab software. CV and LSV measurements were performed at a scan rate of 50 mV s<sup>-1</sup> and 10 mV s<sup>-1</sup>, respectively. Stable CV curves for both HER and ORR activities were recorded after cycling for 30 cycles. After the CV measurement, the LSV curves were recorded with no electrode rotation. A 0.5 M H<sub>2</sub>SO<sub>4</sub> solution saturated with N<sub>2</sub> and O<sub>2</sub> gases was used to evaluate the HER and ORR activities, respectively.

### 3. Results and Discussion

#### 3.1. FE-SEM and TEM Investigations

FE-SEM images of KB and Pt/KB at a magnification of 80,000 $\times$  are displayed in Figure 2a–d. The size of the primary KB particles was approximately 30–50 nm. They exhibited agglomeration into a chain-like structure, which resulted in an interparticle porous and network structure. No difference in morphological structures was observed between KB and Pt/KB, indicating that the plasma did not affect the morphology of the KB supports. However, Pt nanoparticles were not observed in the FE-SEM images because of their small size and low magnification of the images. The presence of Pt nanoparticles on the KB supports was confirmed using EDX analysis. The EDX mapping image (Figure 2e) reveals an even distribution of the Pt signal throughout the investigated area. The EDX spectra in Figure 2f show that the Pt signal was more intense at longer discharge times. This result indicates that the amount of Pt nanoparticles loaded onto KB increased with increasing discharge time. The Pt content deduced from three-area mapping analysis was  $0.16 \pm 0.02$ ,  $0.28 \pm 0.01$ , and  $0.53 \pm 0.11$  atom% for 5-Pt/KB, 10-Pt/KB, and 20-Pt/KB, respectively.

To further elucidate the size and dispersion of Pt nanoparticles on KB, we conducted TEM observations. Figure 3a shows the TEM images of 20-Pt/KB. The Pt nanoparticles (dark contrast) were deposited and distributed on the KB surface (bright contrast). The Pt nanoparticles were determined to be approximately 2–5 nm in diameter. When observed at a high resolution (Figure 3b), the lattice fringes corresponding to the (111) plane of Pt were evident in the region of the Pt nanoparticles,

indicating high crystallinity. Figure 3c shows the selected area electron diffraction (SAED) pattern of 20-Pt/KB. A set of diffraction rings associated with Pt (yellow) and a diffused ring of carbon (red) are visible, which indicates the excellent crystallinity of the Pt nanoparticles and amorphous nature of KB.

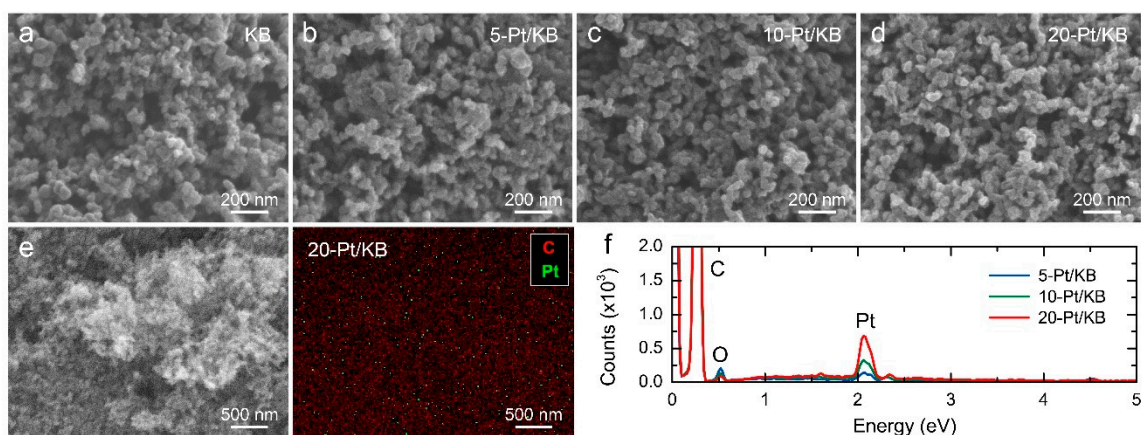


**Figure 2.** FE-SEM images: (a) KB, (b) 5-Pt/KB, (c) 10-Pt/KB, and (d) 20-Pt/KB. (e) energy-dispersive X-ray (EDX) mapping images of 20-Pt/KB. Red and green colors represent the signals of C and Pt, respectively. (f) EDX spectra of 5-Pt/KB, 10-Pt/KB, and 20-Pt/KB.

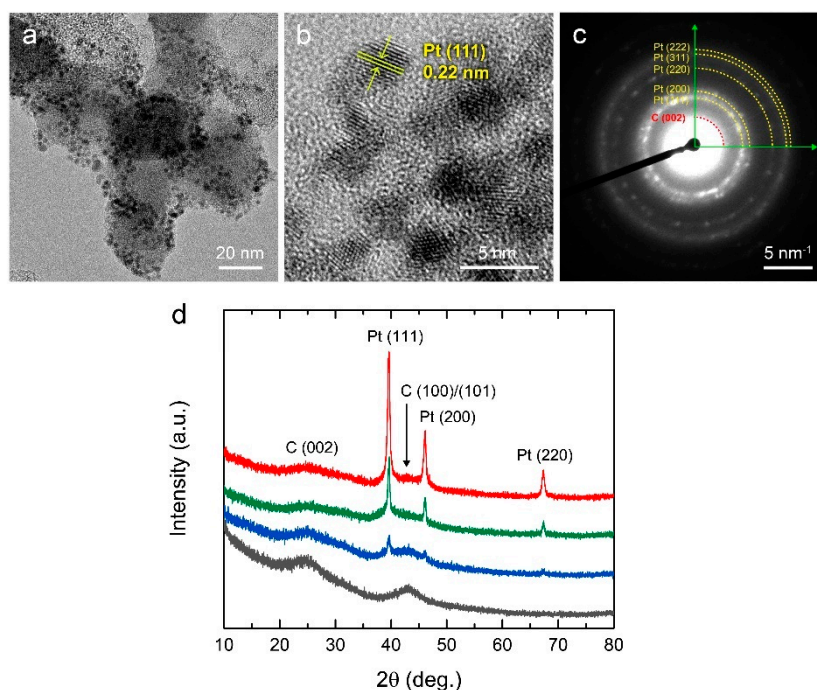


**Figure 3.** (a,b) TEM images, (c) the corresponding selected area electron diffraction (SAED) pattern of 20-Pt/KB, and (d) XRD patterns of all of the investigated catalysts.

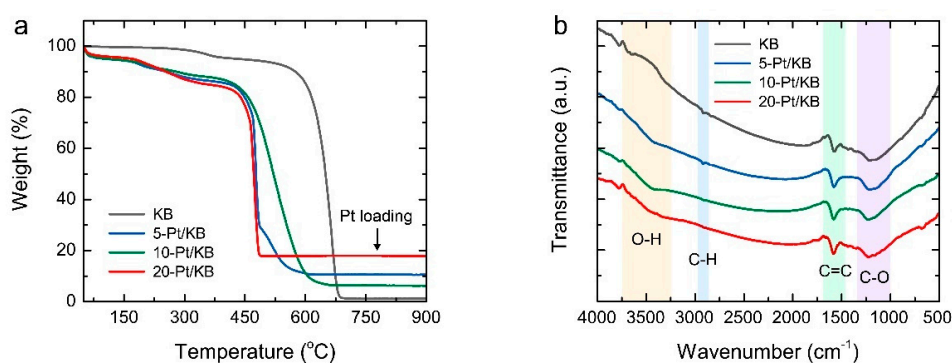
### 3.2. XRD Analysis

Figure 3d demonstrates the XRD patterns of all of the catalysts. The XRD pattern of KB shows a broad peak at  $25.1^\circ$  and a small hump at  $43.1^\circ$ , which are consistent with the graphite (002) and (101) crystallographic planes of carbon, respectively [38]. In the patterns of Pt/KB, in addition to the diffraction peaks of carbon, the characteristic diffraction peaks at  $39.6^\circ$ ,  $46.1^\circ$ , and  $67.3^\circ$  can be indexed to the (111), (200), and (220) crystallographic planes of face-centered cubic-structured Pt (Joint Committee on Powder Diffraction Standards (JCPDS) card no. 70-2057). The sharp diffraction peaks of Pt indicate that it was highly crystalline, which was consistent with the TEM and SAED

results. Moreover, the intensity of the Pt diffraction peaks increased with increasing discharge time, indicating that a greater amount of Pt nanoparticles formed at longer discharge times, which was in accordance with the EDX analysis results.

### 3.3. TG Analysis

Figure 4a shows the TGA curves of all samples upon heating from 50 °C to 900 °C under air flow. The decomposition of pure KB started at approximately 600 °C and was completed at 750 °C. The residual weight of KB at 900 °C was very small (only 1.3 wt%), indicating the high purity of KB. In the case of Pt/KB samples, the residual weight was 5.5, 10.6, and 17.9 wt% for 5-Pt/KB, 10-Pt/KB, and 20-Pt/KB, respectively. The amount of residual weight refers to the loading of Pt nanoparticles on KB. This result is in line with the aforementioned EDX and XRD analyses that the amount of Pt loading increased with increasing discharge time. Moreover, a significant decrease in decomposition temperature with increasing Pt loading was observed. This result implies that Pt could accelerate the decomposition of the KB support owing to a higher oxygen and carbon reaction rate [39,40].



**Figure 4.** (a) TGA curves and (b) FTIR spectra of all of the catalysts.

### 3.4. FTIR Analysis

The surface functional group on the KB surface after plasma exposure was investigated using FTIR measurements, as shown in Figure 4b. All FTIR spectra contained the absorption bands at 3300, 2915, 1580, and 1220 cm<sup>-1</sup> corresponding to O–H stretching, C–H stretching, C=C, and C–O stretching vibration, respectively [41,42]. The FTIR spectra of KB and Pt/KB samples revealed a similar feature, except for the intensity of the O–H peak. A slight increase in intensity of the O–H peak was observed as the discharge time increased. This finding is evidence that the hydroxyl radicals ( $\cdot\text{OH}$ ) generated from the plasma in water and ethanol during synthesis reacted with the surface of the KB support, resulting in the functionalization of –OH groups.

### 3.5. Surface Area and Pore Structure Analyses

Figure 5a presents the N<sub>2</sub> adsorption–desorption isotherms of all catalysts. All isotherms are type II under the International Union of Pure and Applied Chemistry (IUPAC) classification system [43,44]. A large quantity of N<sub>2</sub> was adsorbed at very initial relative pressures ( $P/P_0 < 0.01$ ), indicating the presence of micropores in KB (monolayer formation). As the relative pressure increased, the quantity of adsorbed N<sub>2</sub> gradually increased because of multilayer formation and pore filling. At relative pressures near unity ( $0.95 \leq P/P_0 \leq 0.99$ ), an abrupt increase in the quantity of adsorbed N<sub>2</sub> was observed, which provides the evidence of macropores between agglomerates. A H3-type hysteresis loop in the relative pressure range of 0.40–0.99 was attributed to the effect of capillary condensation in the mesopores [44]. Therefore, KB exhibited a hierarchical porous structure comprising micro, meso, and macropores. As the loading of Pt nanoparticles increased, the isotherm curves shifted toward lower adsorbed quantities, whereas the characteristic feature of isotherms did not change. These results imply a decrease in the surface area at a high loading of Pt nanoparticles. The specific

surface area of all catalysts was determined by the Brunauer–Emmett–Teller (BET) analysis using the  $N_2$  adsorption data in the relative pressure ( $P/P_0$ ) range of 0.05–0.30. As expected, KB exhibited the highest specific surface area of  $1362 \text{ m}^2 \text{ g}^{-1}$ . As the loading of Pt nanoparticles on KB increased, the BET surface area continuously decreased to 1117, 1113, and  $951 \text{ m}^2 \text{ g}^{-1}$  for 5-Pt/KB, 10-Pt/KB, and 20-Pt/KB, respectively. The total pore volume decreased from  $1.74 \text{ cm}^3 \text{ g}^{-1}$  for KB to  $1.27 \text{ cm}^3 \text{ g}^{-1}$  for 20-Pt/KB (Table 1). The pore size distribution was determined from the Barrett–Joyner–Halenda (BJH) model using the  $N_2$  desorption branch, as shown in Figure 5b. The frequency of the occurrence of micropores and small mesopores decreased as the loading of Pt nanoparticles increased. This result is consistent with the change in  $N_2$  adsorption–desorption isotherms showing that the quantity of  $N_2$  adsorbed at the low–relative–pressure region decreased, whereas the hysteresis loop and a steep increase in the quantity of  $N_2$  adsorbed at high relative pressures remained. According to the reduction in total pore volume and decrease in the frequency in the small pore size region from the pore size distribution, the decrease in the specific surface area of Pt/KB could be attributable to the small-sized Pt nanoparticles blocking the pore entrance on the KB surface. These results also imply that the Pt nanoparticles were well-dispersed on the KB supports.

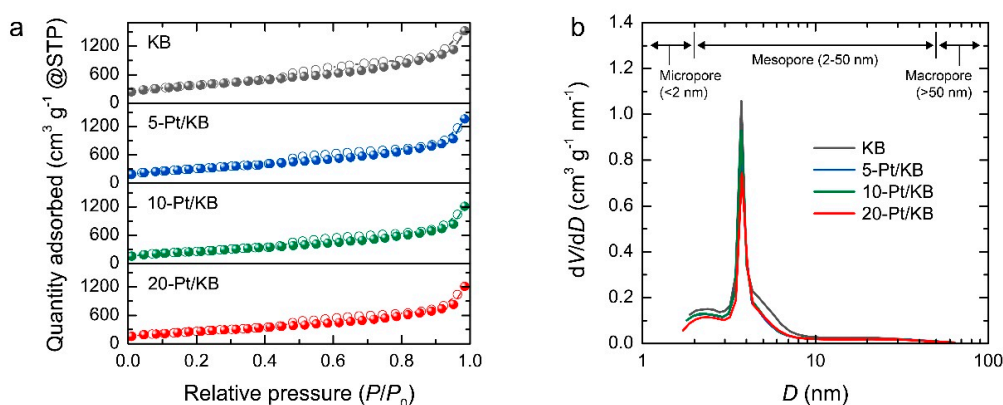


**Figure 5.** Surface area and porosity analyses: (a)  $N_2$  adsorption–desorption isotherms and (b) Barrett–Joyner–Halenda (BJH) pore size distributions determined from the desorption isotherms of all of the catalysts.

**Table 1.** Brunauer–Emmett–Teller (BET) specific surface area ( $S_{BET}$ ), total pore volume ( $V_{total}$ ), and average particle diameter ( $D_{avg}$ ) of all catalysts obtained by the analysis of their  $N_2$  adsorption–desorption isotherms.

Sample	$S_{BET}$ ( $\text{m}^2 \text{ g}^{-1}$ )	$V_{total}$ ( $\text{cm}^3 \text{ g}^{-1}$ )	$D_{avg}$ (nm)
KB	1362	1.74	6.72
5-Pt/KB	1117	1.46	6.98
10-Pt/KB	1113	1.45	7.18
20-Pt/KB	951	1.27	7.20

### 3.6. Electrochemical Measurements

#### 3.6.1. HER Activity

The CV curves of KB, Pt/KB, and commercial 20% Pt/VC, as recorded in a 0.5 M  $H_2SO_4$  solution saturated with  $N_2$  (dashed line) or  $O_2$  gas (solid line), are displayed in Figure 6a. The CV curve of KB in the  $N_2$  saturated solution is featureless, showing no peak. Hydrogen adsorption and desorption peaks were observed for Pt/KB in the potential range of 0.05–0.30 V for the reverse and forward scans, respectively. The electrochemical active surface area (ECSA) can be evaluated by integrating the area under the hydrogen adsorption or desorption peak, which was considered as an indicator of the number of catalytic Pt sites on the catalysts [19,20,23]. We found that the higher loading of Pt nanoparticles on

KB, the larger the area under the hydrogen adsorption or desorption peaks. In Figure 6b, the LSV curve of KB shows a nearly zero current density, indicating no occurrence of HER on KB. For Pt/KB, the LSV curves of HER activity could be divided into two regions. The first region shows zero current because no electrons were exchanged on the catalyst surface, referring to the hydrogen adsorption. The second region is the abrupt change in current density owing to the occurrence of HER ( $2\text{H}^+ + 2\text{e}^- \rightarrow \text{H}_2$ ) [19,20]. The 5-Pt/KB, 10-Pt/KB, 20-Pt/KB, and 20% Pt/VC exhibited almost similar HER onset potentials of approximately  $-0.02$  V, which was comparable with those of other Pt/carbon catalysts reported in the literature (Table S1). Although no difference was observed in the HER onset potential, the current density at  $-0.10$  V was enhanced from  $-74$  mA cm $^{-2}$  for 5-Pt/KB to  $-85$  mA cm $^{-2}$  for 20-Pt/KB.

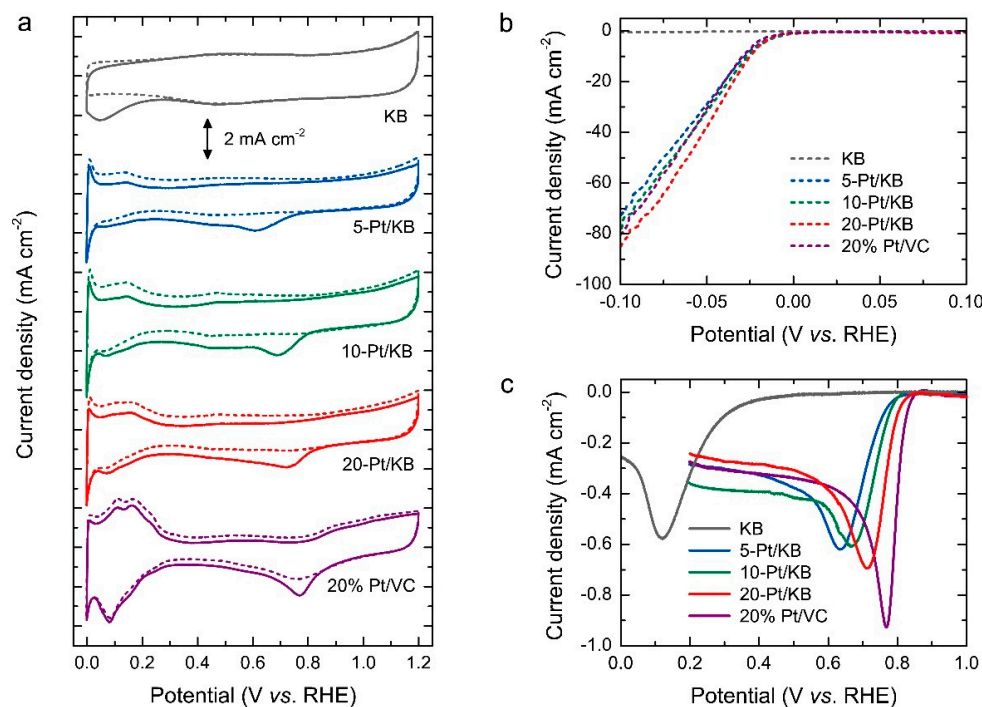


**Figure 6.** Electrochemical measurements: (a) cyclic voltammetry (CV) curves of all the investigated catalysts, as recorded in 0.5 M  $\text{H}_2\text{SO}_4$  solution saturated with  $\text{N}_2$  (dashed line) or  $\text{O}_2$  (solid line). Linear sweep voltammetry (LSV) curves for (b) Hydrogen evolution reaction (HER) and (c) oxygen reduction reaction (ORR) activities of all of the investigated catalysts.

### 3.6.2. ORR Activity

All the CV curves recorded for the electrodes in the  $\text{O}_2$ -saturated solution showed a pronounced cathodic peak, which was not observed in the curve corresponding to the  $\text{N}_2$ -saturated solution. Such a cathodic peak was associated with the occurrence of ORR ( $4\text{H}^+ + \text{O}_2 + 4\text{e}^- \rightarrow 2\text{H}_2\text{O}$ ) on the catalysts. The cathodic peak was located at 0.045 V for KB and positively shifted to 0.724 V for 20-Pt/KB. The LSV measurements were further performed to obtain more information about the ORR onset potential, as shown in Figure 6c. The ORR onset potentials positively shifted toward higher potentials at higher loadings of Pt nanoparticles on KB. The ORR onset potential of 20-Pt/KB was 0.802 V, which was close to that of 20% Pt/VC (0.826 V) and other Pt/carbon catalysts in previous reports (Table S1). However, the ORR peak current of 20-Pt/KB was weaker than that of 20% Pt/VC owing to its lower Pt loading (17.9 wt%). From the electrochemical measurements, we concluded that Pt/KB prepared using SPS exhibited bifunctional catalytic activity for both HER and ORR. The enhanced HER and ORR activities were attributed to a larger amount of Pt nanoparticles on KB, consistent with the findings of several previous works [45–49].

### 3.6.3. HER and ORR Stability

The stability of a catalyst is also an important concern that needs to be considered for practical HER and ORR applications. For the stability tests, 20-Pt/KB was chosen owing to its better catalytic activity toward both HER and ORR than other samples. The commercial 20% Pt/VC was also tested for comparison. The HER stability test was performed by potential cycling between 0 and 1.2 V for 1000 cycles in the N<sub>2</sub>-saturated 0.5 M H<sub>2</sub>SO<sub>4</sub> solution (Figure S1). The area under hydrogen adsorption and desorption of both samples decreased continuously as the number of cycles increased, indicating the reduction in ECSA. Figure 7a,b reveal the LSV curves before and after 1000 cycles for 20-Pt/KB and 20% Pt/VC, respectively. There was a slight change in the LSV curve after 1000 cycles for 20-Pt/KB, whereas a greater decrease in current density was observed for 20% Pt/VC. To further examine the ORR stability of 20-Pt/KB, a potential cycling between 0 and 1.2 V was performed in the O<sub>2</sub>-saturated 0.5 M H<sub>2</sub>SO<sub>4</sub> solution for 1000 cycles (Figure S2). The LSV curves before and after 1000 cycles for 20-Pt/KB and 20% Pt/VC are depicted in Figure 7c,d, respectively. After 1000 cycles, a 46-mV negative shift in the onset potential and a significant reduction in the ORR peak current were clearly observed for 20% Pt/VC. In contrast, the ORR onset potential of 20-Pt/KB negatively shifted by only 35 mV, whereas the ORR peak current dropped slightly. The results obtained from the stability tests are evidence that 20-Pt/KB had more stable HER and ORR activities than 20% Pt/VC. Higher stability of 20-Pt/KB could be attributed to the stronger adhesion between Pt nanoparticles and the KB support, which can be explained by two possible causes: (i) oxygen-containing species and structural defects on the KB surface formed during plasma synthesis can act as favorable anchoring sites for Pt deposition [50–52], and (ii) the Pt nanoparticles produced by SPS were deposited on the KB support with a high kinetic energy owing to acceleration by a high electric field in the plasma region. Therefore, the adhesion of Pt nanoparticles on KB obtained by the SPS method may be stronger than that obtained by other methods, thereby creating a stabilization of Pt nanoparticles against oxidation, dissolution, and/or agglomeration during electrocatalytic reactions.

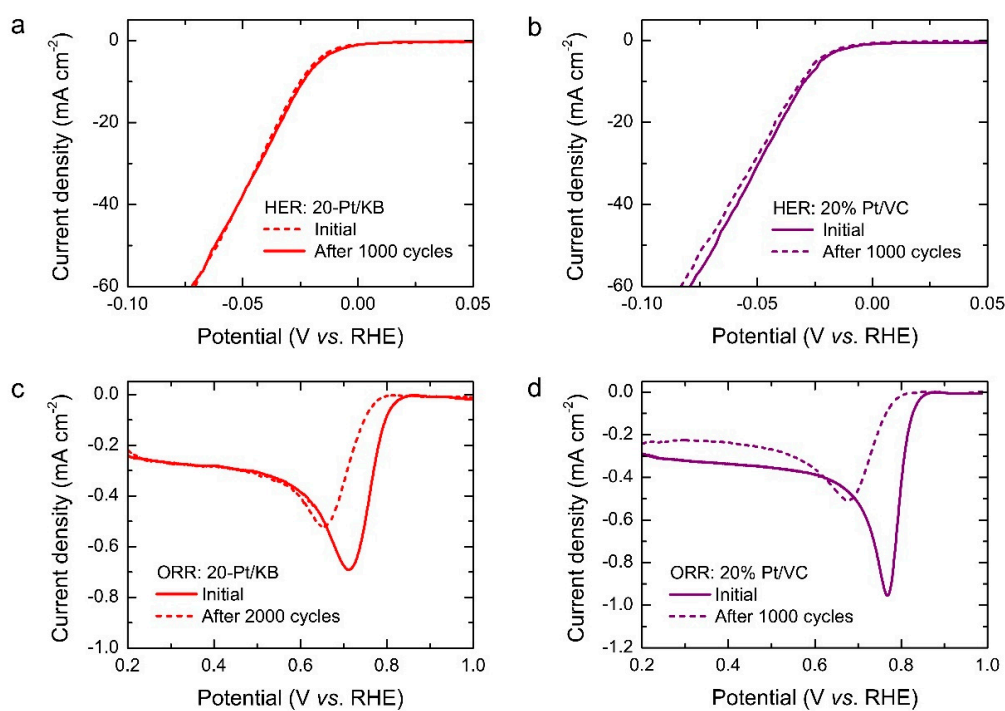


**Figure 7.** LSV curves before and after 1000 cycles for the HER and ORR activities: (a,c) 20-Pt/KB and (b,d) 20% Pt/VC.

#### 4. Conclusions

Pt/KB catalysts were successfully prepared using a fast, facile, and chemical-free SPS method. The loading of Pt nanoparticles sputtering from the electrodes onto KB increased from 5.5 to 17.9 wt% with increasing discharge time (from 5 to 20 min). The plasma did not influence the morphology of KB and Pt/KB, even at longer discharge times. TEM and XRD analysis results show that the 2–5-nm Pt nanoparticles were well-crystallized and evenly distributed on the KB surface. The deposition of Pt nanoparticles on the KB supports resulted in blocking of the pore entrance at the KB surface, reducing the specific surface area. From the electrochemical measurements in a 0.5 M H<sub>2</sub>SO<sub>4</sub> solution, all Pt/KB catalysts exhibited bifunctional catalytic activity toward HER and ORR, which enhanced with increasing discharge time or Pt loading. The HER and ORR activities of 20-Pt/KB (17.9 wt%) were found to be nearly close to that of commercial 20% Pt/VC. In HER and ORR stability tests, 20-Pt/KB was more stable than 20% Pt/VC owing to the strong interaction between Pt nanoparticles and KB. The results obtained in this work provide useful reference information and support for preparing bifunctional Pt/KB catalysts for HER and ORR. Moreover, the SPS method shows strong potential as an alternative green synthesis method for preparing noble metal nanoparticles on a broad range of supports for various purposes in catalysis applications.

**Supplementary Materials:** The following are available online at <http://www.mdpi.com/2504-477X/4/3/121/s1>, Figure S1: CV curves at different cycles measured in N<sub>2</sub>-saturated 0.5 M H<sub>2</sub>SO<sub>4</sub> solution: (a) 20-Pt/KB and (b) 20% Pt/VC, Figure S2: CV curves at different cycles measured in O<sub>2</sub>-saturated 0.5 M H<sub>2</sub>SO<sub>4</sub> solution: (a) 20-Pt/KB and (b) 20% Pt/VC.

**Author Contributions:** Conceptualization, G.P.; methodology, C.M.-L., C.H. and G.P.; formal analysis, C.M.-L. and C.H.; investigation, C.M.-L. and C.H.; resources, G.P.; data curation, C.M.-L., C.H. and G.P.; writing—original draft preparation, C.M.-L. and C.H.; writing—review and editing, G.P.; visualization, G.P.; supervision, G.P.; project administration, G.P. All authors have read and agreed to the published version of the manuscript.

**Funding:** This research was funded by the Faculty of Engineering, Kasetsart University and the International Collaborative Education Program for Materials Technology, Education and Research (ICE-Matter) Consortium, Association of Southeast Asian Nations (ASEAN) University Network/Southeast Asia Engineering Education Development Network (AUN/SEED-Net), Japan International Cooperation Agency (JICA).

**Acknowledgments:** The authors would like to thank Nagahiro Saito, Department of Chemical Systems Engineering, for providing a bipolar pulse power supply for this research; Jidapa Chantaramethakul, student at the Department of Materials Engineering, Kasetsart University for her TEM investigation; Kasetsart University Research and Development Institute (KURDI) for financial support for the proofreading service fee.

**Conflicts of Interest:** The authors declare no conflict of interest.

#### References

1. Kannan, N.; Vakeesan, D. Solar energy for future world: A review. *Renew. Sustain. Energy Rev.* **2016**, *62*, 1092–1105. [[CrossRef](#)]
2. Joselin Herbert, G.M.; Iniyar, S.; Sreevalsan, E.; Rajapandan, S. A review of wind energy technologies. *Renew. Sustain. Energy Rev.* **2007**, *11*, 1117–1145. [[CrossRef](#)]
3. Khan, I.U.; Othman, M.H.D.; Hashim, H.; Matsuura, T.; Ismail, A.F.; Rezaei-DashtArzhandi, M.; Wan Azelee, I. Biogas as a renewable energy fuel—A review of biogas upgrading, utilisation and storage. *Energy Convers. Manag.* **2017**, *150*, 277–294. [[CrossRef](#)]
4. Andrews, J.; Shabani, B. The role of hydrogen in a global sustainable energy strategy. *Wiley Interdiscip. Rev. Energy Environ.* **2014**, *3*, 474–489. [[CrossRef](#)]
5. Staffell, I.; Scamman, D.; Abad, A.V.; Balcombe, P.; Dodds, P.E.; Ekins, P.; Shah, N.; Ward, K.R. The role of hydrogen and fuel cells in the global energy system. *Energy Environ. Sci.* **2019**, *12*, 463–491. [[CrossRef](#)]
6. Fernández-Moreno, J.; Guelbenzu, G.; Martín, A.J.; Folgado, M.A.; Ferreira-Aparicio, P.; Chaparro, A.M. A portable system powered with hydrogen and one single air-breathing PEM fuel cell. *Appl. Energy* **2013**, *109*, 60–66. [[CrossRef](#)]
7. Pollet, B.G.; Kocha, S.S.; Staffell, I. Current status of automotive fuel cells for sustainable transport. *Curr. Opin. Electrochem.* **2019**, *16*, 90–95. [[CrossRef](#)]

8. Van de Kaa, G.; Scholten, D.; Rezaei, J.; Milchram, C. The battle between battery and fuel cell powered electric vehicles: A BWM approach. *Energies* **2017**, *10*, 1707. [[CrossRef](#)]
9. Felseghi, R.-A.; Carcadea, E.; Raboaca, M.S.; Trufin, C.N.; Filote, C. Hydrogen fuel cell technology for the sustainable future and stationary applications. *Energies* **2019**, *12*, 4593. [[CrossRef](#)]
10. Zhang, C.; Shen, X.; Pan, Y.; Peng, Z. A review of Pt-based electrocatalysts for oxygen reduction reaction. *Front. Energy* **2017**, *11*, 268–285. [[CrossRef](#)]
11. Li, Y.; Li, Q.; Wang, H.; Zhang, L.; Wilkinson, D.P.; Zhang, J. Recent progresses in oxygen reduction reaction electrocatalysts for electrochemical energy applications. *Electrochem. Energy Rev.* **2019**, *2*, 518–538. [[CrossRef](#)]
12. Shao, Y.; Dodelet, J.-P.; Zelenay, P. PGM-free cathode catalysts for PEM fuel cells: A mini-review on stability challenges. *Adv. Mater.* **2019**, *31*, 1807615. [[CrossRef](#)] [[PubMed](#)]
13. Haryanto, A.; Fernando, S.; Murali, N.; Adhikari, S. Current status of hydrogen production techniques by steam reforming of ethanol: A review. *Energy Fuels* **2005**, *19*, 2098–2106. [[CrossRef](#)]
14. Kalamaras, C.M.; Efstathiou, A.M. Hydrogen production technologies: Current state and future developments. *Conf. Pap. Energy* **2013**, *2013*, 690627. [[CrossRef](#)]
15. Hu, C.; Zhang, L.; Gong, J. Recent progress made in the mechanism comprehension and design of electrocatalysts for alkaline water splitting. *Energy Environ. Sci.* **2019**, *12*, 2620–2645. [[CrossRef](#)]
16. Zou, X.; Zhang, Y. Noble metal-free hydrogen evolution catalysts for water splitting. *Chem. Soc. Rev.* **2015**, *44*, 5148–5180. [[CrossRef](#)]
17. Felderhoff, M.; Weidenthaler, C.; Von Helmolt, R.; Eberle, U. Hydrogen storage: The remaining scientific and technological challenges. *Phys. Chem. Chem. Phys.* **2007**, *9*, 2643–2653. [[CrossRef](#)]
18. Alswad, A.; Baroutaji, A.; Achour, H.; Carton, J.; Al Makky, A.; Olabi, A.G. Developments in fuel cell technologies in the transport sector. *Int. J. Hydrogen Energy* **2016**, *41*, 16499–16508. [[CrossRef](#)]
19. Eftekhari, A. Electrocatalysts for hydrogen evolution reaction. *Int. J. Hydrogen Energy* **2017**, *42*, 11053–11077. [[CrossRef](#)]
20. Dubouis, N.; Grimaud, A. The hydrogen evolution reaction: From material to interfacial descriptors. *Chem. Sci.* **2019**, *10*, 9166–9181. [[CrossRef](#)]
21. Sui, S.; Wang, X.; Zhou, X.; Su, Y.; Riffat, S.; Liu, C.-J. A comprehensive review of Pt electrocatalysts for the oxygen reduction reaction: Nanostructure, activity, mechanism and carbon support in PEM fuel cells. *J. Mater. Chem. A* **2017**, *5*, 1808–1825. [[CrossRef](#)]
22. Ren, X.; Lv, Q.; Liu, B.; Wang, Y.; Liu, A.; Wu, G. Current progress of Pt and Pt-based electrocatalysts used for fuel cells. *Sustain. Energy Fuels* **2020**, *4*, 15–30. [[CrossRef](#)]
23. Nguyen, H.D.; Nguyen, T.T.L.; Nguyen, K.M.; Ha, T.H.; Nguyen, Q.H. Preparation of the Vulcan XC-72R-supported Pt nanoparticles for the hydrogen evolution reaction in PEM water electrolyzers. *Adv. Nat. Sci. Nanosci. Nanotechnol.* **2015**, *6*, 025012. [[CrossRef](#)]
24. Lee, K.; Zhang, J.; Wang, H.; Wilkinson, P. Progress in the synthesis of carbon nanotube- and nanofiber-supported Pt electrocatalysts for PEM fuel cell catalysis. *J. Appl. Electrochem.* **2006**, *36*, 507–522. [[CrossRef](#)]
25. Begum, H.; Kim, Y.-B. Improvement of catalytic activity of platinum nanoparticles decorated carbon graphene composite on oxygen electroreduction for fuel cells. *Processes* **2019**, *7*, 586. [[CrossRef](#)]
26. Hsieh, B.-J.; Tsai, M.-C.; Pan, C.-J.; Su, W.-N.; Ricj, J.; Lee, J.F.; Yang, Y.-W.; Hwang, B.-J. Platinum loaded on dual-doped TiO<sub>2</sub> as an active and durable oxygen reduction reaction catalyst. *NPG Asia Mater.* **2017**, *9*, e403. [[CrossRef](#)]
27. Stepanov, A.L.; Golubev, A.N.; Nikitin, S.I.; Osin, Y.N. A review on the fabrication and properties of platinum nanoparticles. *Rev. Adv. Mater. Sci.* **2014**, *38*, 160–175.
28. Jeyaraj, M.; Gurunathan, S.; Qasim, M.; Kim, J.-H. A Comprehensive review on the synthesis, characterization, and biomedical application of platinum nanoparticles. *Nanomaterials* **2019**, *9*, 1719. [[CrossRef](#)] [[PubMed](#)]
29. Park, J.Y.; Aliaga, C.; Renzas, J.R.; Lee, H.; Somorjai, G.A. The role of organic capping layers of platinum nanoparticles in catalytic activity of CO oxidation. *Catal. Lett.* **2009**, *129*, 1–6. [[CrossRef](#)]
30. Niu, Z.; Li, Y. Removal and utilization of capping agents in nanocatalysis. *Chem. Mater.* **2014**, *26*, 72–83. [[CrossRef](#)]
31. Safo, I.A.; Dosche, C.; Özaskan, M. Effects of capping agents on the oxygen reduction reaction activity and shape stability of Pt nanocubes. *ChemPhysChem* **2019**, *19*, 3010–3023. [[CrossRef](#)] [[PubMed](#)]

32. Hu, X.; Cho, S.-P.; Takai, O.; Saito, N. Rapid synthesis and structural characterization of well-defined gold clusters by solution plasma sputtering. *Cryst. Growth Des.* **2012**, *12*, 119–123. [[CrossRef](#)]
33. Hu, X.; Takai, O.; Saito, N. Simple synthesis of platinum nanoparticles by plasma sputtering in water. *Jpn. J. Appl. Phys.* **2013**, *52*, 01AN05. [[CrossRef](#)]
34. Panomsuwan, G.; Chataramethakul, J.; Chokradjaroen, C.; Ishizaki, T. In situ solution plasma synthesis of silver nanoparticles supported on nitrogen-doped carbons with enhanced oxygen reduction activity. *Mater. Lett.* **2019**, *251*, 135–139. [[CrossRef](#)]
35. Shi, J.; Hu, X.; Zhang, J.; Tang, W.; Li, H.; Shen, X.; Saito, N. One-step facile synthesis of Pd nanoclusters supported on carbon and their electrochemical property. *Prog. Nat. Sci. Mater. Int.* **2014**, *24*, 593–598. [[CrossRef](#)]
36. Kang, J.; Saito, N. In situ solution plasma synthesis of mesoporous nanocarbon-supported bimetallic nanoparticles. *RSC Adv.* **2015**, *5*, 29131–29134. [[CrossRef](#)]
37. Panomsuwan, G.; Ueno, T.; Yui, H.; Nakamura, J.; Saito, N. Chapter 7: Solution plasma reactions and materials synthesis. In *Molecular Technology, Volume 3: Materials Innovation*, 1st ed.; Yamamoto, H., Kato, T., Eds.; Wiley-VCH: Weinheim, Germany, 2019; pp. 137–172.
38. Holade, Y.; Morais, C.; Servat, K.; Napporn, T.K.; Kkokoh, K.B. Enhancing the available specific surface area of carbon supports to boost the electroactivity of nanostructured Pt catalysts. *Phys. Chem. Chem. Phys.* **2014**, *16*, 25609–25620. [[CrossRef](#)]
39. Baturina, O.A.; Aubuchon, S.R.; Wynne, K.J. Thermal stability in air of Pt/C catalysts and PEM fuel cell catalyst layers. *Chem. Mater.* **2006**, *18*, 1498–1504. [[CrossRef](#)]
40. Chen, X.; Wang, H.; Wang, Y.; Bai, Q.; Gao, Y.; Zhang, Z. Synthesis and electrocatalytic performance of multi-component nanoporous structure alloy for direct methanol fuel cells. *Catalysts* **2015**, *5*, 1003–1015. [[CrossRef](#)]
41. Hood, Z.D.; Yang, X.; Li, Y.; Naskar, A.K.; Chi, M.; Paranthaman, M. Conversion of waste tire rubber into high-value-added carbon support for electrocatalysis. *J. Electrochem. Soc.* **2018**, *165*, H881–H888. [[CrossRef](#)]
42. Tucureanu, V.; Matei, A.; Avram, A.M. FTIR spectroscopy for carbon family study. *Crit. Rev. Anal. Chem.* **2006**, *46*, 502–520. [[CrossRef](#)] [[PubMed](#)]
43. Sing, K.S.W.; Everett, D.H.; Haul, E.A.W.; Moscou, L.; Pierotti, R.A.; Rouquérol, J.; Siemieniewska, T. Reporting physisorption data for gas/solid systems with special reference to the determination of surface area and porosity. *Pure Appl. Chem.* **1985**, *57*, 603–619. [[CrossRef](#)]
44. Sing, K.S.W.; Williams, R.T. Physisorption hysteresis loops and the characterization of nanoporous materials. *Adsorp. Sci. Technol.* **2004**, *22*, 733–782. [[CrossRef](#)]
45. Soboleva, T.; Zhao, X.; Malek, K.; Xie, Z.; Navessin, T.; Holdcroft, S. On the micro-, meso-, and macroporous structures of polymer electrolyte membrane fuel cell catalyst layers. *ACS Appl. Mater. Interfaces* **2010**, *2*, 375–384. [[CrossRef](#)] [[PubMed](#)]
46. Stevens, D.A.; Dhan, J.R. Electrochemical characterization of the active surface in carbon-supported platinum electrocatalysts for pemfuel cells. *J. Electrochem. Soc.* **2003**, *150*, A770–A775. [[CrossRef](#)]
47. Taylor, S.; Fabbri, E.; Levecque, P.; Schmidt, T.J.; Conrad, O. The effect of platinum loading and surface morphology on oxygen reduction activity. *Electrocatalysis* **2016**, *7*, 287–296. [[CrossRef](#)]
48. Jukk, K.; Kongi, N.; Tammeveski, K.; Arán-Ais, R.M.; Solla-Gullón, J.; Feliu, J.M. Loading effect of carbon-supported platinum nanocubes on oxygen electroreduction. *Electrochim. Acta* **2017**, *251*, 155–166. [[CrossRef](#)]
49. Ghanim, A.H.; Koonce, J.G.; Hasa, B.; Rassoolkhani, J.M.; Cheng, W.; Peate, D.W.; Lee, J.; Mubeen, S. Low-loading of Pt nanoparticles on 3D carbon foam support for highly active and stable hydrogen production. *Front. Chem.* **2018**, *6*, 523. [[CrossRef](#)]
50. Tiwari, J.N.; Pan, F.-M.; Chen, T.-M.; Tiwari, R.N.; Lin, K.-L. Electrocatalytic activity of Pt nanoparticles electrodeposited on amorphous carbon-coated silicon nanocones. *J. Power Sources* **2010**, *195*, 729–735. [[CrossRef](#)]
51. Karthikeyan, N.; Vunayan, B.P.; Rajesh, M.; Balaji, K.; Subramani, A.K.; Ramaprabhu, S. Highly durable platinum based cathode electrocatalysts for PEMFC application using oxygen and nitrogen functional groups attached nanocarbon supports. *Fuel Cells* **2015**, *15*, 278–287. [[CrossRef](#)]
52. Bao, X.; Gong, Y.; Chen, Y.; Zhang, H.; Wang, Z.; Mao, S.; Xie, L.; Jiang, Z.; Wang, Y. Carbon vacancy defect-activated Pt cluster for hydrogen generation. *J. Mater. Chem. A* **2019**, *7*, 15364–15370. [[CrossRef](#)]

